MNE 19 (2023) 100212

Contents lists available at ScienceDirect

Micro and Nano Engineering

journal homepage: www.sciencedirect.com/journal/micro-and-nano-engineering

Characterisation and modelling of nonlinear resonance behaviour on very-high-frequency silicon nanoelectromechanical resonators

Fang Ben [a,*], James Fernando [a], Jun-Yu Ou [b], Cécilia Dupré [c], Eric Ollier [c], Faezeh Arab Hassani [a,1], Hiroshi Mizuta [a,2], Yoshishige Tsuchiya [a,*]

[a] School of Electronics and Computer Sciences, University of Southampton, Highfield Campus, Southampton SO17 1BJ, United Kingdom
[b] School of Physics & Astronomy, University of Southampton, Southampton, Highfield Campus, Southampton SO17 1BJ, United Kingdom
[c] CEA-Leti, 38054 Grenoble, France

A R T I C L E I N F O

Keywords:
Nanoelectromechanical systems
Nonlinear resonance
Mixing measurements
Duffing oscillator equation

A B S T R A C T

This paper reports a novel method to build a model for nonlinear resonance behaviour of very-high-frequency (VHF) silicon nanoelectromechanical (NEM) resonators, measured via 1-ω mixing resonance measurements. Systematic fitting results for the experimental data of a 1.5-μm-long beams have been achieved with explicit explanation of the amount of intrinsic mechanical nonlinearity and nonlinear voltage-tuning effect. Asymmetric line shape and onset of hysteresis on nonliner resonance behavour have been well demonstrated with less fitting errors. The development of a modelling method of nanoscale resonator devices which includes nonlinear response is beneficial for seamless technology transfer from individual devices to integrated systems in the future.

1. Introduction

Nonlinear responses of micro- and nano-electromechanical (MEM/NEM) resonators have been well documented since the first experimental observation of nonlinear MEM resonance, reported by Andres et al. [1] in 1987, and then in recent years are attracting much more attention in NEM resonators as nonlinear resonance regime can be easily reached thanks to their small mass and size [2]. While nonlinear behaviours are generally considered undesirable characteristics of common micro- and nanoelectromechanical systems (MEMS/NEMS) when operated in the linear regime, there have been some cases reported where nonlinear characteristics are actively utilised to improve the performance of devices, or even required to achieve desireble functionality. Sansa et al. [3] proved a concept of a nonlinear detection scheme which amplified the resonance response and enhanced the dynamic range for sensing applications. To implement a neural network by using coupled MEM oscillator arrays, nonlinear behaviour of MEM resonators with hysteric characteristics is suggested to play a pivotal role in fading memory functionality [4]. An alternative approach of developing neural computing hardware based on nolinear MEM oscillators has also been proposed [5,6].

This trend strongly suggests that detailed analysis of nonlinear dynamic behaviour of MEM/NEM resonators is important. In particular, towards highly-integrated MEM/NEM resonator arrays for neuromorphic computing or active system-level integration of MEMS/NEMS sensor arrays for Internet-of-Things (IoT) applications, it is very important to develop analytical or mathematical models to describe the operation of MEN/NEM resonators, including their nonlinear behaviour with a certain level of accuracy.

Silicon NEMS devices possess great technological advantage in terms of integration capability as their fabrication processes are designed well compatible with advanced Si-based integrated circuits (IC) technologies [7]. Since the first demonstration of Si NEMS resonators in ultra-high-sensitivity mass sensors [8,9], ultra-low-leakage current switches [10,11] and in-plane resonators on a silicon-on-insulator (SOI) platform, which is compatible with complementary metal-oxide-semiconductor (CMOS) technology [7,12], are among those devices developed to extend Si NEMS. We have fabricated doubly-clamped silicon NEM

---

* Corresponding authors.
E-mail addresses: F.Ben@soton.ac.uk (F. Ben), yt2@ecs.soton.ac.uk (Y. Tsuchiya).

[1] Present address: Department of Electrical and Electronic Engineering, University of Bristol, Woodland Road, BS8 1UB Bristol, United Kingdom.

[2] Present address: School of Materials Science, Japan Advanced Institute of Science and Technology, Nomi, Ishikawa 923-1292, Japan.

https://doi.org/10.1016/j.mne.2023.100212
Received 9 January 2023; Received in revised form 2 May 2023; Accepted 22 May 2023

resonators on an SOI platform with CMOS-compatible processes and reported in-plane resonance characteristics [13] and out-of-plane resonance with their fundamental-mode resonance frequencies of up to 330 MHz, which is over the higher end of the very-high-frequency (VHF) band (30–300 MHz) [14]. Recently, the nonlinear resonance behaviour of doubly-clamped Si NEM resonators has been measured via a frequency modulation (FM) detection method and analysed by comparing with the nonlinear Duffing oscillator equation to develop systematic and accurate models of nonlinear NEM resonators [15]. Further details of the modelling procedure for the FM detection data will be published elsewhere.

1-ω mixing measurement is an alternative method to detect the resonance behaviour of NEM resonators by using the NEM resonator as a mixer of radio frequency (RF) signals, where the data analysis is found to be much simpler than that in the FM method. In this paper, we develop a novel model for the solutions of NEM resonators nonlinear dynamics characerisation and successfully implement it to the analysis of nonlinear resonance for a 1.5-μm-long silicon NEM beam with 1-ω mixing measurement. The correspondence between the dimensional or material parameters of physical silicon NEMS resonators fabricated on SOI-CMOS platform and the physical parameters appearing in the Duffing equation will be discussed systematically. Our discussion will include an analysis of characteristic hysteric behaviours and of the conversion coefficient between the detected current and the displacement of the beam.

2. Mathematical model for nonlinear NEM resonators

Fig. 1(a) shows a schematic diagram of a NEM resonator which we focus on this study. A doubly-clamped silicon suspended beam is placed in proximity to three electrodes: a back electrode from the substrate and two side electrodes which are laterally alighed with the beam. Only the back electrode is used in this study to actuate out-of-plane motion of the beam, to be modelled in the following. Due to the ultra-small size of the suspended beam, the external driving force should be large enough to achieve the required signal-to-noise ratio between the resonant and off-resonant states, resulting in the regime with the largest amplitude of vibrating motion, where nonlinearity has to be taken into account. In general, nonlinearity stems from various sources such as the mechanical properties of materials, geometrical asymmetry, or types of external driving force, as has been investigated previously in [5,6,13–15].

Our modelling starts from the one-degree-of-freedom universal equation of motion,

$$m_b\ddot{x}(t) + C\dot{x}(t) + Kx(t) = F_{elec} \tag{1}$$

where m_b is the effective mass, C is the damping coefficient, K is the measure of stiffness, and F_{elec} is the external electrostatic driving force. The effective mass m_b of a doubly-clamped silicon nanobeam with a surrounding SiO_2 layer is obtained from the similar analysis reported in [8] in detail. The damping coefficient C is substituted by $\omega_0 m_b/Q$, where ω_0 is the mechanical resonance frequency and Q is the quality factor. At the nanoscale, energy dissipation from the resonator can come from different damping sources which are primarily contributed by fluidic or gas, anchor, and thermoelastic damping. The effect by fluidic dissipation can be computed via boundary integral equation (BIE) proposed by [16] and further simplified and validated by [17,18] where anchor and thermoelastic damping model for MEMS have been reported by [19]. In particular, all of the above reported damping models are closely linked with the deformation and proportional to the package air pressure. Details about the dissipation model and temperature dependence can be found in [13,14], which used identical NEM resonators to those described in this paper. The quality factor is considered to be constant for same sample with a fixed temperautre (300K) and vacuum pressure (3×10^{-2} mbar) in this study.

By following the approach presented in [5,13], the restoring force $Kx(t)$ is written into a perturbation series as,

$$Kx(t) = k_0\left[x(t) + k_1x(t)^2 + k_2x(t)^3 + \ldots + k_nx(t)^{n+1} + \ldots\right] \tag{2}$$

where k_0 is the linear stiffness coefficient and k_n is defined as a stiffness coefficient of an $xn+1$ term. The even-order restoring energy ($n = 2$, 4, 6 …) is cancelled out due to the symmetry of the structure, while the displacement $x(t)$ remains less comparable to the initial gap g_0, so the higher order terms of $n > 4$ are negligible. The remaining $x(t)^3$ term

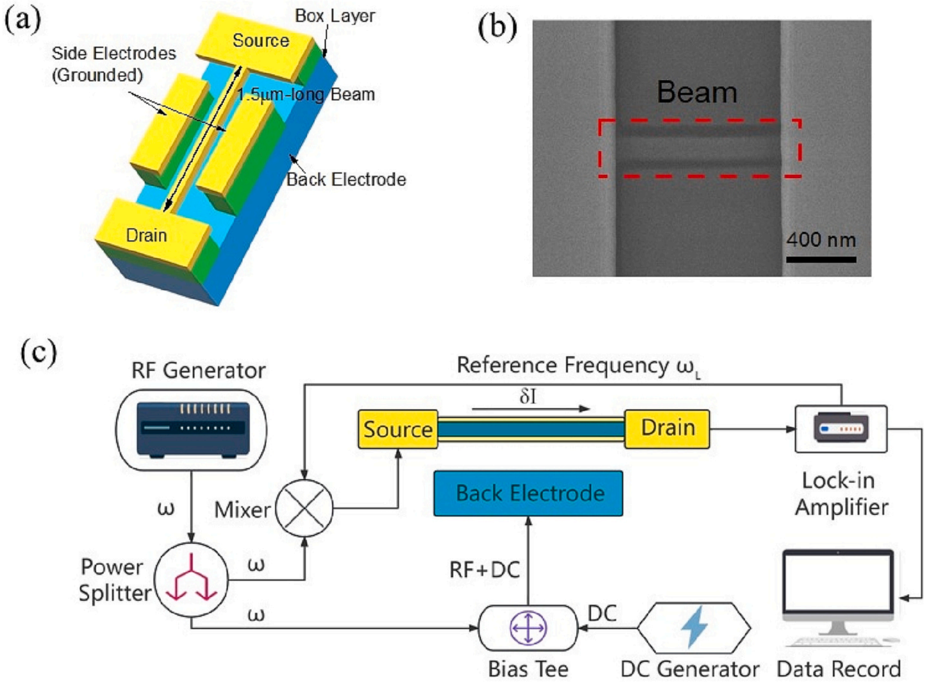

Fig. 1. (a) A schematic of a NEM resonator. The designed SOI thickness is 45 nm. (b) An SEM image of a 1.5-μm-long beam. (c) A 1-ω-mixing measurement diagram. V_{DC}, V_{AC}, and V_L are the actuation voltage, RF, and modulation signal amplitudes, respectively. ω_L is the modulation frequency.

represents the nonlinearity derived from the mechanical stiffness term and the cofficient k_2 is equivalent to the mechanical nonlinear stiffness β_m.

The external force is induced via capacitive coupling between the suspended beam and the backside electrode where DC and AC voltages are applied (See the 1-ω measurement diagram in Fig. 1 (b)). The electrostatice force F_{elec} is with the change of capacitance due to the motion of the beam, therefore can be expressed as a function of DC bias voltage V_{DC}, driving AC voltage V_{AC}, and with the gap $g = g_0 - x(t)$,

$$F_{elec} = \frac{\varepsilon_0 S V_{DC}(V_{DC}+V_{AC})}{[g_0 - x(t)]^2} = \frac{\varepsilon_0 S V_{DC}(V_{DC}+V_{AC})}{{g_0}^2}\left[\frac{1}{g_0} + \ldots + \frac{n}{{g_0}^n}x(t)^n\right] \tag{3}$$

where ε_0 is the vacuum permittivity, S is the cross-sectional area of the capacitance, g_0 is the initial gap distance, and the equation is expanded about $x = 0$. For the same reason discussed for Eq. 1, F_{elec} can be simplified as,

$$F_{elec} = F^0_{elec} + \frac{2\varepsilon_0 S V_{DC}(V_{DC}+V_{AC})}{{g_0}^3}x(t) + \frac{4\varepsilon_0 S V_{DC}(V_{DC}+V_{AC})}{{g_0}^5}x(t)^3 \tag{4}$$

where F^0_{elec} is the initial term of F_{elec} in time domain. The coefficients of $x(t)$ and $x(t)^3$ are defined as k_e and β_e, which are the equivalent electrical linear and nonlinear stiffnesses, respectively. Eq. (1) can be re-written as,

$$x(t)'' + \frac{\omega_0}{Q}x(t)' + \omega_0^2 x(t) - k_e x(t) + \omega_0^2\beta_m x(t)^3 - \beta_e\, x(t)^3 = \frac{F^0_{elec}}{m_b} \tag{5}$$

$$k_e = \frac{2\varepsilon_0 S V_{DC}(V_{DC}+V_{AC})}{m_b {g_0}^3}, \beta_e = \frac{4\varepsilon_0 S V_{DC}(V_{DC}+V_{AC})}{m_b {g_0}^5} \tag{6}$$

Note that the coefficient of $x(t)$, $\omega_0^2 - k_e$, is related to the shift of resonance peak position under biasing, whereas the coefficient of $x(t)^3$, $\omega_0^2\beta_m - \beta_e$ represents the degree of nonlinearity which can be tuned by external voltage.

There are various approaches to solving the nonlinear ordinary differential equation (ODE) as Eq. (5). Besides commonly used computational method like harmonic balance and 4th Runge-Kutta, Frangi's group [18,20–24] have made a consistent effort at using a continuation approach to study nonlinear characteristics for various MEMS designs. The definition of arclength control enables the continuation approach to be a versatile method to simulate the dynamics of MEMS with high nonlinearity, allowing the intermedia solution to be visible in simulation. Homotopy analysis method (HAM) is a similar ODE solving approach that uses a pre-defined controller to trace the final solutions from initial guesses with assistance from Newton-Raphson iteration [25,26]. This paper employs a numerical method called the Petrov-Galerkin (P-G) method to obtain an approximated solution of Eq. (5), which is known to be ideal for solving differential equations for a symmetric system that contains odd-order terms only and to convert the system function to another domain [27]. Hence, this feature makes the P-G method intrinsically suitable to solve the problem in this paper, as Eq. (5) is a time-domain equation and the target fitting model is for frequency-domain analysis.

Here we use a test function $x(t) = A(\omega)cos(\omega t) + B(\omega)sin(\omega t)$, where $A(\omega)$ and $B(\omega)$ are frequency-dependent coefficients of two orthogonal components for $x(t)$. The P-G method focuses on minimising weighted residuals, in this case, the residual work. For a steady-state symmetric oscillation, the total residual work in each periodic oscillation cycle is balanced to be zero [15,26,28]. From Eq. (5), the instantaneous residual force $R(t)$ is defined as,

$$R(t) = \left[x(t)'' + \frac{\omega_0}{Q}x(t)' + \omega_0^2 x(t) - k_e x(t) + \omega_0^2\beta_m x(t)^3 - \beta_e\, x(t)^3\right] - \frac{F^0_{elec}}{m_b} \tag{7}$$

Therefore, the residual work is a product of the residual force and the displacement, which is expressed as

$$R(t)x(t) = R(t)A(\omega)cos(\omega t) + R(t)Bsin(\omega t). \tag{8}$$

By integrating Eq. (8) through a period of $2\pi/\omega$, we obtain

$$\begin{aligned} G_1(A,B,\omega) &= \int_0^{\frac{2\pi}{\omega}} R(t)A(\omega)cos(\omega t)dt = 0 \\ G_2(A,B,\omega) &= \int_0^{\frac{2\pi}{\omega}} R(t)B(\omega)sin(\omega t)dt = 0 \end{aligned} \tag{9}$$

where $G_1(A,B,\omega)$ and $G_2(A,B,\omega)$ are two orthogonal functions of the residual work per cycle, which are equal to zero.

A set of two equations as functions of A, B, and ω in Eq. (9) can be solved numerically by using Newton-Raphson iteration [29]. The iteration equation is written as

$$[A_{N+1}(\omega)\ B_{N+1}(\omega)] = [A_N(\omega)\ B_N(\omega)] - \frac{\boldsymbol{G}}{\boldsymbol{J}}, \tag{10}$$

where $\boldsymbol{G}, \boldsymbol{J}$ are the matrix (G_1, G_2) and the Jacobian matrix of $\boldsymbol{G}$, respectively.

$$\boldsymbol{J} = \begin{pmatrix} \frac{\partial G_1}{\partial A}(A,B,\omega) & \frac{\partial G_1}{\partial B}(A,B,\omega) \\ \frac{\partial G_2}{\partial A}(A,B,\omega) & \frac{\partial G_2}{\partial B}(A,B,\omega) \end{pmatrix} \tag{11}$$

After a number of iterations $N = 500$, steady-state approximate solutions for A and B as a function of ω are obtained and the absolute value of the displacement, $|x(\omega)|$ is expressed as $|x(\omega)| = \sqrt{A(\omega)^2 + B(\omega)^2}$.

3. Experimental methods and analysis

NEMS resonator samples used in this study were fabricated by SOI-CMOS compatible process with top-down hybrid electron-beam/deep-ultraviolet (EB/DUV) lithography. Fabrication detail can be found in [14]. The beam consists of n-type heavily-doped silicon with doping concentration of doping concentration of 4×10^{19} cm^3 and surrounding thermal SiO$_2$ layer. The designed dimensions of the silicon nanobeams are 1.5 μm in length, 45 nm in thickness, and 105 or 135 nm in width. An SEM image of a 1.5-μm-long NEM resonator sample is shown in Fig. 1 (b), showing a successful definition of nanoscale Si suspended beam structure.

Fig. 1 (c) shows a schematic diagram of a 1-ω mixing measurement system to detect the resonance of NEM resonators. An RF signal with the frequency ω, generated by Agilent N5181A MXG signal generator, is split into two by the power splitter. One is fed to a bias tee where the RF signal is combined with DC bias, generated by an Agilent B1500A seimconductor device analyser, and then applied to the back electrode of a NEM resonator. Another is connected to a mixer, where a reference signal $V_{\omega L}$ with the frequency of ω_L, generated by a Stanford Research Systems SR830 DSP lock-in amplifier, is mixed and then routed to the input electrode for the suspended nanobeam. The output electrode of the beam is connected to the lock-in amplifier to detect the current modulation of the beam for the frequency ω_L. The conductance change results from the change of the induced charge δQ in the beam, given by $\delta Q = \delta(C_g V_g) = C_g \delta V_g + V_g \delta C_g$, where C_g is the capacitance between gate and beam, and where V_g is the constant part of the signal V_{DC} applied at the back electrode, δV_g is the varying signal applied on the back electrode, which is V_{AC} [30]. The change of charge δQ is a sum of the standard transistor gating effect $C_g V_{AC}$, which is modulated by the changing of the back electrode signal and the change of capacitance due to the motion of the beam [30]. The current modulated due to the conductance change is detected by using the NEM beam as a mixer. The change of the current is the product of the beam signal δV_{Beam} and the conductance δG, which can be expressed as follows [30],

$$\delta I = \delta G \delta V_{Beam} = \frac{1}{2\sqrt{2}} \frac{\delta G}{\delta V_g} \left(V_{AC} + V_{DC} \frac{\delta C_g}{C_g} \right) \delta V_{Beam} \tag{12}$$

in terms of the transconductance $\delta G / \delta V_g$ and the gate-beam capacitance modulation $\delta C_g / C_g$. V_{Beam} is the signal applied to the beam. At the resonance, the capacitance modulation is enhanced due to the increase of the beam displacement, resulting in the appearance of a peak of the current modulation signal at the resonance with respect to the frequency sweep. Eq. (12) is used to link between the current modulation data which were obtained experimentally and the theoretically-deduced displacement value in the follwing comparative study. The displacement simulated by using the model displayed in the last seciton contributes the change of capacitance δC_g, leading to the final calculation of δI. Given the frequency control ω, the current-frequency response δI can be obtained accordingly, and then used for the fitting of experimental data to extract key parameters ω_0, Q, β_m by giving avaliable fitting parameters such as dimensional parameters L, W, thickness, g_0, and experimental conditions V_{DC}, V_{AC}.

4. Results and discussion

Prior to measuement of resonance behaviour and subsequent comparison with the theoretical model, we estimated the transconductance $\delta G / \delta V_g$ by using the background baseline noise current I_{bg} of a NEM resonator at off-resonance [31], detected by the lock-in amplifier without applying V_{DC}. I_{bg} is derived from Eq. (12) with $V_{DC} = 0$ as

$$\left| I_{bg} \right| = \frac{1}{2\sqrt{2}} \frac{\delta G}{\delta V_g} \left| V_{Beam} \right| \bullet \left| V_{AC} \right| \tag{13}$$

I_{bg} of a NEM resonator with L = 1.5 μm and W = 105 nm has been measured with increasing applied RF power and plotted in Fig. 2. Because the value of V_{Beam} is a product of AC and reference signals, the I_{bg} shall be proportional to V_{AC}^2. Taking $V_{AC}{}^2$ as a horizontal axis, the clear linear relationship between I_{bg} and $V_{AC}{}^2$ indicates the transconductance $\delta G / \delta V_g$ is constant in this power range. With $V_{\omega_L} = 50$ mV, the transconductance $\delta G / \delta V_g$ is estimated to be 54.5 nS/V, which will be used in subsequent data analysis. Note that we assume $\delta G / \delta V_g$ at $V_{DC} = 0$ is not changed with applying V_{DC} in our heavily doped conductive silicon beam.

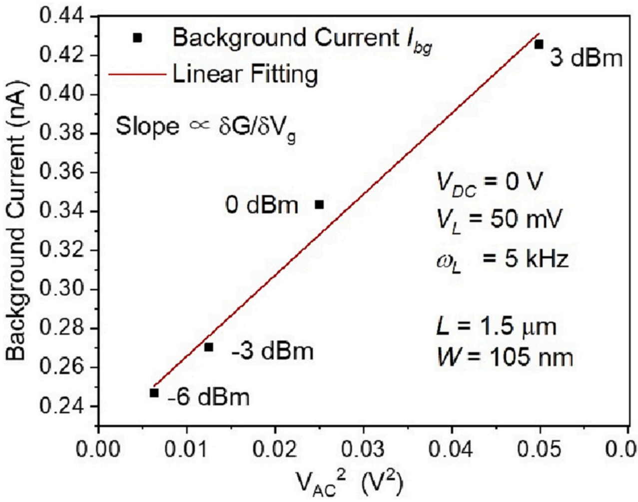

Fig. 2. Background signal versus V_{AC}. $\delta G / \delta V_g$ is extracted from the linear fitting.

Fig. 3 (a) presents how the resonance lineshape is developed with changing V_{DC} for the modulation current of the NEM resonator with $L =$ 1.5 μm and $W =$ 105 nm. Marks plotted in Fig. 3 (a) are experimental data. At $V_{DC} = 3$ V, the resonance appears at around 124.1 MHz and then the resonance frequency is shifted leftwards with increase of V_{DC}. Note that the current amplitude at the resonance has increased with increasing V_{DC}, from 830 pA to 2.47 nA when V_{DC} is increased from 3 V to 6 V. Fig. 3(b) summarises the V_{DC} dependence of the resonance frequency and amplitude of the current modulation. The red solid lines in Fig. 3 (a) are curves fitted with the numerical solutions of the Duffing equation (Eq. (5)). The well-fitted results suggest our approximated solutions can explain well how the resonance is changed with respect to the actuation voltage V_{DC}. The downshift of the frequency with the application of V_{DC} corresponds to the effects of equivalent electrical linear stiffness k_e. The total amount of stiffness is characterised as a coefficient of the $x(t)$ term in Eq. (5), which is $\omega_0^2 - k_e$. With increasing V_{DC}, k_e increases according to Eq. (6) so that the total amount of linear stiffness is decreased, resulting in the leftward shift of the resonance. This is an electrical softening effect. The increase of the current amplitude with increasing V_{DC} is also consistent with Eq. (12), where the V_{DC} increase contributes directly, as well as the increase of increase of electrostatic force, leading to further displacement of the beam and then modulation of the capacitance.

A set of graphs in Fig. 4 display the result of resonance characteristics of the 1.5-μm-long and 105-nm-wide NEM resonator beam under varied RF power P, which has the unit of dBm. For each fixed V_{DC} of 3, 4, 5, and 6 V (Fig. 4 (a) – (d)), the RF power is changed from 2 dBm to 10 dBm with a step of 2 dBm, and each lineshape of resonance curve for the current amplitude is plotted accordingly with respect to the frequency. Again, marks are based on experimental data, whereas the red lines are based on the numerical solution of the Duffing equation (Eq. (5)). For all four groups of RF power dependence in Fig. 4 (a) – (d) under different V_{DC}, the current amplitude increases with increasing the RF power. Looking into the details, in Fig. 4 (a), the resonance frequency moves slightly higher with the increase of power, which corresponds to a linear hardening effect. This effect is still observed at $V_{DC} = 4$ V in Fig. 4 (b). On the other hand at $V_{DC} = 5$ V in Fig. 4 (c), the resonance curve with higher RF power starts showing assymmetry and the top of the peak tends to bend towards lower frequencies. This is commonly known as Duffing nonlinear softening effect, which is observed more explicitly in Fig. 4 (d) at $V_{DC} = 6$ V. Strength of nonlinearity is directly proportional to the displacement according to Bartsch et al. [32], which is consistent with our observation that nonlinear behaviour becomes more prominent with increasing V_{DC} and RF power. Note that the aforementioned P-G numerical method does not consider the case where the beam is under a driving frequency $\omega = 0$. In this case, the beam is no longer driven by RF and the deflection is solely due to the static force with respect to the existing DC. We have employed the Euler-Bernoulli model to investigate the static deflection, having $EI\left(d^4 y / dx^4\right) = F_{elec}^0(\omega = 0)$, where $E, I, y(x)$ are Young's modulus of silicon, the moment of inertia for rectangular cross-section of the beam, and the static deflection solutions of the beam, respectively. The equation has been solved numerically to obtain the deflection solutions with respect to V_{DC}. Results show the static deflection is quadratically proportional to V_{DC} and the maximum static deflection is 37.7 pm when V_{DC} is 2 V, which is far less than the nanometre scale deflection at resonance.

It is noticeable that our model fitting results are consistent with the experimental data throughout the RF power variation in this study. The nonlinear equivelant electrical stiffness β_e, defined Eq. (6), can explain how nonlinearity can be tuned by changing V_{DC} and V_{AC}. Another key parameter representing the nonlinearity is the mechanical nonlinear stiffness β_m, which denotes the intrinsic amount of nonlinearity from the

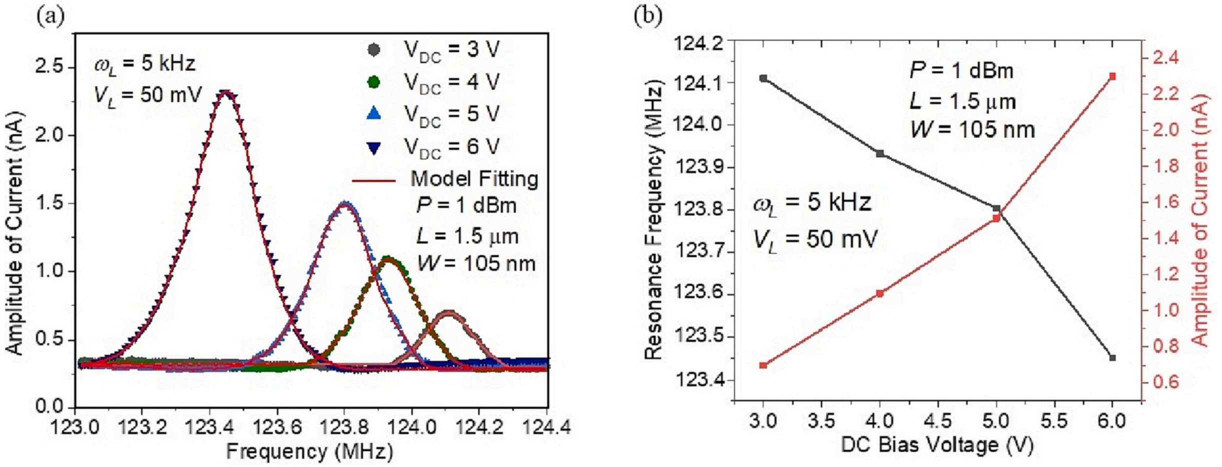

Fig. 3. (a) DC bias dependence of the resonance line shape. (b) A summary of how the resonance frequency and peak current change with respect to the DC bias.

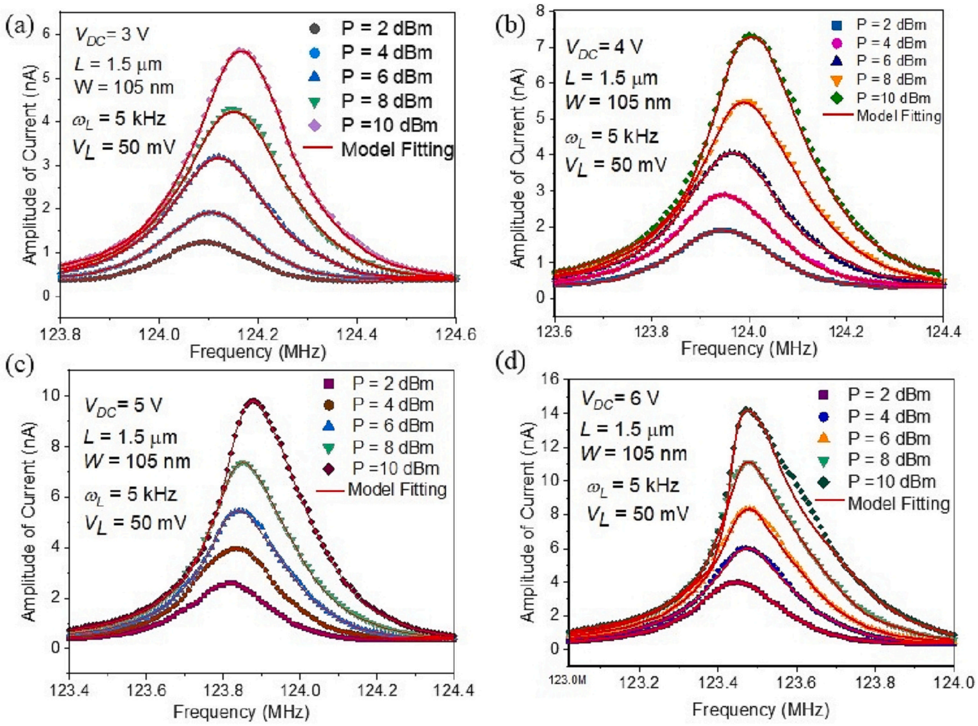

Fig. 4. Power dependence of the resonance line shape at varying DC bias at (a) 3 V, (b) 4 V, (c) 5 V, and (d) 6 V.

mechanical structure of the device. Without changing the dimensions, design and material of the device, β_m is considered to remain constant theoretically. Upon this hypothesis, we have successfully obtained β_m as a fitting parameter in current fitting of the whole four groups of power dependence data with resprct to the fitting variables of V_{DC} and V_{AC}.

For the purpose of validation of the method, we use another NEM resonator sample with a slightly wider beam ($L = 1.5$ μm, $W = 135$ nm) and apply the identical approach to extract the fitting parameters in our analysis, the resonance frequency ω_0, quality factor Q, and the mechanical nonlinear stiffness β_m. Table 1 summarises the parameters extracted from the fitting results for the two samples with different widths. The transconductance of the sample where $W = 135$ nm is also estimated from the baseline noise. The wider beam shows a higher resonance frequency and a slightly lower quality factor, corresponding to the increase of stiffness, and has a higher transconductance which is consistent with the increase of conductive cross-sectional area. As for the mechanical nonlinearity stiffness β_m, a relatively large negative value for a wider beam could be linked with the increase of overall stiffness of the beam as well. Overall, throughout the comparison of the fitting results between two different NEM resonator samples, we have confirmed very good consistency between the experimental results and numerical solutions.

Table 1
A summary of extracted parameters in fitting for 1.5-μm-long beams with different designed widths.

Width(nm)	105	135
ω_0 (MHz)	125.38	127.62
Q	~560	~528
$\beta_m\left(\mathrm{m}^{-2}\right)$	-5.58×10^{-5}	-7.72×10^{-5}
$\delta G/\delta V$(nS/V)	~54.5	~63.3

Hysteric behaviour is known to appear in nonlinear resonance when a larger external force is applied. The hysteresis stems from the fundamental bifurcation of a nonlinear system where multiple stable states can exist simultaneously. According to [1] the onset of hysteresis can be defined as a point where the shift of resonance peak due to nonlinearity is just about to exceed the bandwidth. For a Duffing oscillator system with an x^3 term, two stable states plus one intermediate state are considered to occur at the vicinity of bifurcation regime [33]. This often leads to a seperation of resonance curves between the data taken with the frequency swept upward and downward. The mechanism of the P-G method focuses on the equilibrium point when integrating the residual energy, and therefore, only stable branches of the hysteresis can be simulated in our model. For the study of unstable branches, [18] reported their simulation by using continuation appraoch to analyse MEMS nonlinear hysteric dynamics. In our case, the model is for the preparation of further applications that utilise the bi-stability of MEMS/NEMS for neuromorphic computing. In addition, only stable branches can be obtained from experiment, hence, this paper will only focus on the fitting with respect to the stable solutions of hysteresis, where the intermedia unstable solution will be considered in the future. Fig. 5 (a) – (c) shows how hysteric behaviour is developed with the increasing of the power at the fixed V_{DC} of 8 V. Blue and red open circles represent experimental data from a forward frequency sweep and a backward frequency sweep, respectively. By extracting the maximum and minimum solutions of the Duffing equation in Eq. (5), the experimental data with hysteresis are successfully fitted as the red lines in Fig. 5 (a) – (c). Fig. 4 (d) shows how the resonance frequencies are shifted in the hysteric regime with respect to the RF power. The separation of two resonance frequencies becomes larger with increasing the RF power, leading to the frequency difference of 0.5 MHz at $P = 12$ dBm.

The Relative Root Mean Square Error (RRMSE) is introduced to evaluate this method by quantifying the difference between experimental and numerical data as a fitting error. RRMSE is defined as,

$$RRMSE = \frac{\sqrt{\frac{1}{n}\sum_{i=1}^{n}\left(\overline{I}_{exp}^{i} - \overline{I}_{model}^{i}\right)^{2}}}{\sum_{i=1}^{n}\overline{I}_{exp}^{i}} \times 100\% \tag{14}$$

where $\overline{I}_{exp}^{i}$ and $\overline{I}_{model}^{i}$ are the i-th point of experimental data and model simulation data, respectively. Compared with a common error parameter such as the root mean square error (RMSE), RRMSE is more versatile to apply for comparison between different discrete set of data. By applying this error evaluation method for the 1-ω mixing measurement data taken in the study, RRMSE of 4.72% are evaluated. The fitting accuracy is considered to be excellent when RRMSE is <10% based on the RRMSE criteria given by [34].

Our method provides with a new solution that can explain the experimental data from existing silicon-based doubly-clamped silicon NEM resonators with the resonance frequency in the VHF range of up to 120 MHz. Structural and material parameters are provided experimentally, whereas the Duffing equation is solved numerically under the specific condition where the external force is applied electrically to the oscillator via capacitive coupling. As a result, V_{DC} dependence, RF power dependence, and hysteric behavour of nonlinear resonance of NEM resonators have been consistently well explained. For advancing the development of silicon-based integrated systems for various applications such as neuromorphic information processing or IoT devices, simple and accurate modelling of individual devices becomes more important. We believe this attempt is a key first step of model development for NEM resonator/oscillator devices by including their behaviour in nonlinear regime.

5. Conclusion

We have built a mathematical model for nonlinear resonance behaviour of very-high-frequency (VHF) silicon nanoelectromechanical (NEM) resonators. Electrostatic force, to be applied in 1-ω mixing

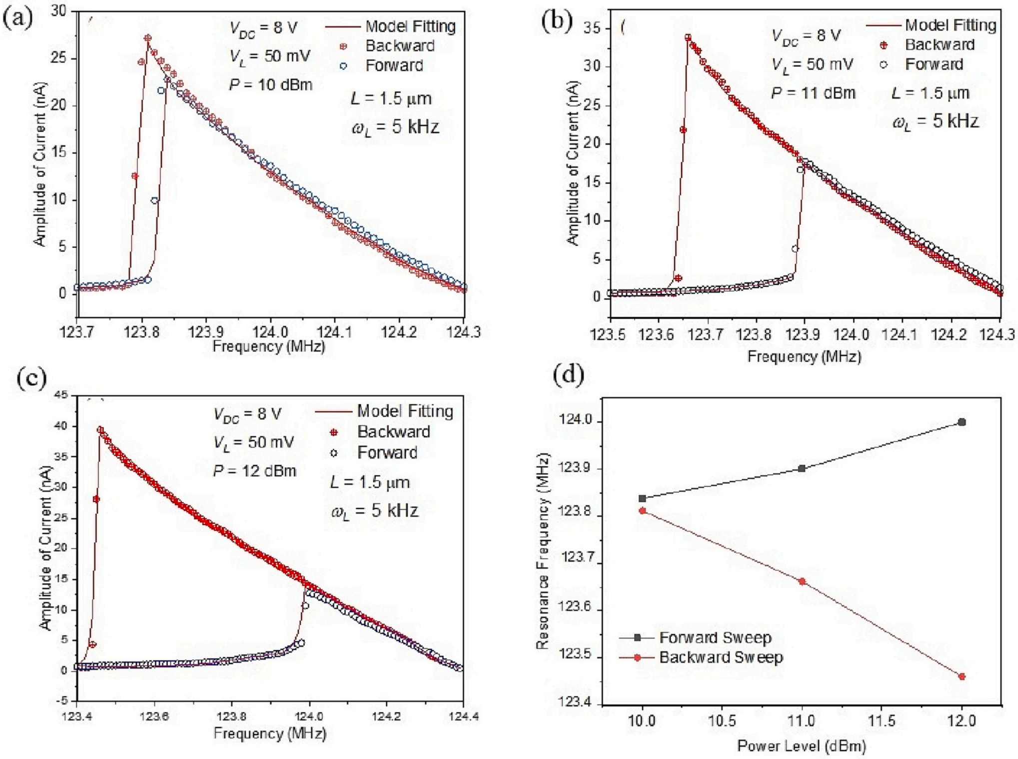

Fig. 5. Hysteresis behaviour observed experimentally is plotted with the power level at (a)10 dBm, (b)11 dBm, (c)12 dBm, respectively. (d) A summary shows the difference of resonance frequency in power dependence with respect to forward frequency sweep and backward frequency sweep.

resonance measurements has been incorporated into the Duffing oscillator equation, which is solved numerically via the Petrov-Galerkin and Newton-Raphson methods to fit a set of experimental data with variation of the actuation DC voltage and RF power. Systematic fitting results for the resonance data of 1.5-μm-long beams, with reasonable fitting parameters, have successfully traced the characteristic asymmetric line shape and the onset of hysteresis at around the frequency of 125 MHz for the first time. The numerical results are compared with a set of experimental data by adjusting the resonance frequency ω_0, quality factor Q, mechanical nonlinear coefficient β_m. With the value of β_m obtained from the fitting, the overall amount of nonlinearity can be analysed quantitatively by giving the expression of equivalent electrical nonlinearity β_e. Two stable solutions of the Duffing equation in the hysteric regime enable the model to be fitted with bi-stability, and thus be used to investigate the bifurcation phenomenon. Fitting errors are evaluated via the calculated RRMSE, showing a good alignment between our model and 1-ω mixing measurement result. This work can be a key step towards the development of an accurate and simple device model for NEM resonators.

Declaration of Competing Interest

The authors declare that they have no known competing financial interests or personal relationships that could have appeared to influence the work reported in this paper.

Data availability

Data will be made available on request.

Acknowledgements

This work was partially supported by the EU FP7-ICT project NEMSIC [grant number 224525] and the CHIST-ERA grant NOEMIA [CHIST-ERA-21-NOEMS-004] by the Engineering and Physical Sciences Research Council [grant number EP/X03495X/1].

References

[1] M.V. Andres, K.W.H. Foulds, M.J. Tudor, Nonlinear vibrations and hysteresis of micromachined silicon resonators designed as frequency-out sensors, Electron. Lett. 23 (18) (1987) 952–954, https://doi.org/10.1049/el:19870670.

[2] N. Ghaemi, A. Nikoobin, M.R. Ashory, A comprehensive categorization of micro/nanomechanical resonators and their practical applications from an engineering perspective: a review, Adv. Electron. Mater. 8 (11) (2022) 2200229, 11/01 2022.

[3] M. Sansa, V. Nguyen, S. Baguet, C. Lamarque, R. Dufour, S. Hentz, Real time sensing in the non linear regime of nems resonators, in: 2016 IEEE 29th International Conference on Micro Electro Mechanical Systems (MEMS), 24–28 Jan. 2016, 2016, pp. 1050–1053, https://doi.org/10.1109/MEMSYS.2016.7421814.

[4] J.C. Coulombe, M.C.A. York, J. Sylvestre, Computing with networks of nonlinear mechanical oscillators, PLoS One 12 (6) (2017), e0178663, https://doi.org/10.1371/journal.pone.0178663.

[5] M. Rafaie, M.H. Hasan, F.M. Alsaleem, Neuromorphic MEMS sensor network, Appl. Phys. Lett. 114 (16) (2019) 163501, https://doi.org/10.1063/1.5081804, 04/22 2019.

[6] F.M. Alsaleem, M.H.H. Hasan, M.K. Tesfay, A MEMS nonlinear dynamic approach for neural computing, J. Microelectromech. Syst. 27 (5) (2018) 780–789, https://doi.org/10.1109/JMEMS.2018.2864175.

[7] S. Chong, et al., Integration of nanoelectromechanical (NEM) relays with silicon CMOS with functional CMOS-NEM circuit, in: 2011 International Electron Devices Meeting, 5–7 Dec. 2011, 2011, https://doi.org/10.1109/IEDM.2011.6131645, pp. 30.5.1–30.5.4.

[8] K.L. Ekinci, Y.T. Yang, M.L. Roukes, Ultimate limits to inertial mass sensing based upon nanoelectromechanical systems, J. Appl. Phys. 95 (5) (2004) 2682–2689, https://doi.org/10.1063/1.1642738, 03/01 2004.

[9] E. Mile, et al., In-plane nanoelectromechanical resonators based on silicon nanowire piezoresistive detection, Nanotechnology 21 (16) (2010) 165504, https://doi.org/10.1088/0957-4484/21/16/165504, 03/30 2010.

[10] D.A. Czaplewski, et al., A nanomechanical switch for integration with CMOS logic, J. Micromech. Microeng. 19 (8) (2009) 085003, https://doi.org/10.1088/0960-1317/19/8/085003, 07/09 2009.

[11] H. Lin, C. Kuo, G. Li, C. Su, T. Huang, Operation of a novel device with suspended nanowire channels, IEEE Electron Dev. Lett. 31 (5) (2010) 384–386, https://doi.org/10.1109/LED.2010.2041744.

[12] A. Koumela, et al., High frequency top-down junction-less silicon nanowire resonators, Nanotechnology 24 (43) (2013) 435203, https://doi.org/10.1088/0957-4484/24/43/435203, 10/09 2013.

[13] A.F. Hassani, Y. Tsuchiya, H. Mizuta, In-plane resonant Nano-electro-mechanical sensors: a comprehensive study on design, fabrication and characterization challenges, Sensors 13 (7) (2013), https://doi.org/10.3390/s130709364.

[14] Y. Tsuchiya, et al., Characteristic resonance features of SOI-CMOS-compatible silicon nanoelectromechanical doubly-clamped beams up to 330 MHz, in: 2018 IEEE Micro Electro Mechanical Systems (MEMS), 21–25 Jan. 2018, 2018, pp. 515–518, https://doi.org/10.1109/MEMSYS.2018.8346603.

[15] F. Ben, J. Fernando, J.-Y. Ou, Y. Tsuchiya, Development of systematic fitting model for nonlinear nanoelectromechanical resonance analysis, in: 2021 IEEE 34th International Conference on Micro Electro Mechanical Systems (MEMS), 25–29 Jan. 2021, 2021, pp. 611–614, https://doi.org/10.1109/MEMS51782.2021.9375461.

[16] P. Fedeli, A. Frangi, Integral equations for free-molecule ow in MEMS: recent advancements, Commun. Appl. Indus. Math. 8 (1) (2017) 67–80, https://doi.org/10.1515/caim-2017-0004.

[17] P. Fedeli, A. Frangi, G. Laghi, G. Langfelder, G. Gattere, Near vacuum gas damping in MEMS: simplified modeling, J. Microelectromech. Syst. 26 (3) (2017) 632–642, https://doi.org/10.1109/JMEMS.2017.2686650.

[18] V. Zega, et al., Numerical modelling of non-linearities in MEMS resonators, J. Microelectromech. Syst. 29 (6) (2020) 1443–1454, https://doi.org/10.1109/JMEMS.2020.3026085.

[19] M.W.U. Siddiqi, P. Fedeli, C. Tu, A. Frangi, J.E.Y. Lee, Numerical analysis of anchor loss and thermoelastic damping in piezoelectric AlN-on-Si lamb wave resonators, J. Micromech. Microeng. 29 (10) (2019) 105013, https://doi.org/10.1088/1361-6439/ab392c, 08/27 2019.

[20] A. Frangi, A. Guerrieri, N. Boni, Accurate simulation of parametrically excited micromirrors via direct computation of the electrostatic stiffness, Sensors 17 (4) (2023), https://doi.org/10.3390/s17040779.

[21] A. Frangi, G. Gobat, Reduced order modelling of the non-linear stiffness in MEMS resonators, Int. J. Non-linear Mech. 116 (2019) 211–218, 11/01/ 2019.

[22] G. Gobat, V. Zega, P. Fedeli, L. Guerinoni, C. Touzé, A. Frangi, Reduced order modelling and experimental validation of a MEMS gyroscope test-structure exhibiting 1:2 internal resonance, Sci. Rep. 11 (1) (2021) 16390, 08/12 2021.

[23] Y. Shen, N. Béreux, A. Frangi, C. Touzé, Reduced order models for geometrically nonlinear structures: assessment of implicit condensation in comparison with invariant manifold approach, Eur. J. Mech. A/Solids 86 (2021), 104165, 03/01/2021.

[24] G. Gobat, V. Zega, P. Fedeli, C. Touzé, A. Frangi, Frequency combs in a MEMS resonator featuring 1:2 internal resonance: ab initio reduced order modelling and experimental validation, Nonl. Dyn. 111 (4) (2023) 2991–3017, https://doi.org/10.1007/s11071-022-08029-7, 02/01 2023.

[25] F. Tajaddodianfar, M.R.H. Yazdi, H.N. Pishkenari, Nonlinear dynamics of MEMS/NEMS resonators: analytical solution by the homotopy analysis method, Microsyst. Technol. 23 (6) (2017) 1913–1926, 06/01 2017.

[26] N. Herisanu, B. Marinca, V. Marinca, Nonlinear vibration of double-walled carbon nanotubes subjected to mechanical impact and embedded on Winkler–Pasternak Foundation, Materials 15 (23) (2023).

[27] J. Reddy, An Introduction to the Finite Element Method, McGraw-Hill New York, 2004.

[28] C.A.J. Fletcher, Computational Galerkin Methods, in: C.A.J. Fletcher (Ed.), Computational Galerkin Methods, Springer Berlin Heidelberg, Berlin, Heidelberg, 1984, pp. 72–85.

[29] E. Süli, D.F. Mayers, An Introduction to Numerical Analysis, Cambridge University Press, Cambridge, 2003.

[30] V. Sazonova, Y. Yaish, H. Üstünel, D. Roundy, T.A. Arias, P.L. McEuen, A tunable carbon nanotube electromechanical oscillator, Nature 431 (7006) (2004) 284–287, 09/01 2004.

[31] M. Sansa, M. Fernández-Regúlez, J. Llobet, Á. San Paulo, F. Pérez-Murano, High-sensitivity linear piezoresistive transduction for nanomechanical beam resonators, Nat. Commun. 5 (2014) 4313, 07/07/online.

[32] S.T. Bartsch, M. Arp, A.M. Ionescu, Junctionless silicon nanowire resonator, IEEE J. Electron Dev. Soc. 2 (2) (2014) 8–15.

[33] S. Tiwari, R.N. Candler, Using flexural MEMS to study and exploit nonlinearities: a review, J. Micromech. Microeng. 29 (8) (2019), 083002, 06/10 2019.

[34] M. Despotovic, V. Nedic, D. Despotovic, S. Cvetanovic, Evaluation of empirical models for predicting monthly mean horizontal diffuse solar radiation, Renew. Sust. Energ. Rev. 56 (2016) 246–260, 04/01/ 2016.